nature communications

Article

https://doi.org/10.1038/s41467-025-56315-w

# Electron–phonon coupling and coherent energy superposition induce spin-sensitive orbital degeneracy for enhanced acidic water oxidation

Received: 12 August 2024

Accepted: 15 January 2025

Yanfeng Shi[1,2,3], Lupeng Wang[1,3], Miao Liu[1,3], Zuozheng Xu[2], Peilin Huang[2], Lizhe Liu[2] & Yuanhong Xu[1]

The development of acid-stable water oxidation electrocatalysts is crucial for high-performance energy conversion devices. Different from traditional nanostructuring, here we employ an innovative microwave-mediated electron–phonon coupling technique to assemble specific Ru atomic patterns (instead of random Ru-particle depositions) on $Mn_{0.99}Cr_{0.01}O_2$ surfaces ($Ru_{MW}$-$Mn_{1-x}Cr_xO_2$) in $RuCl_3$ solution because hydrated Ru-ion complexes can be uniformly activated to replace some Mn sites at nearby Cr-dopants through microwave-triggered energy coherent superposition with molecular rotations and collisions. This selective rearrangement in $Ru_{MW}$-$Mn_{1-x}Cr_xO_2$ with particular spin-differentiated polarizations can induce localized spin domain inversion from reversed to parallel direction, which makes $Ru_{MW}$-$Mn_{1-x}Cr_xO_2$ demonstrate a high current density of 1.0 A $cm^{-2}$ at 1.88 V and over 300 h of stability in a proton exchange membrane water electrolyzer. The cost per gallon of gasoline equivalent of the hydrogen produced is only 43% of the 2026 target set by the U.S. Department of Energy, underscoring the economic significance of this nanotechnology.

The development of hydrogen economy is pivotal for the future of decarbonizing the energy landscape. The International Energy Agency predicts that global hydrogen production could reach 14% of final energy demand by 2050[1]. Achieving this goal depends on producing green hydrogen affordably on an industrial scale. Proton exchange membrane water electrolysis (PEM-WE)[2] and alkaline water electrolysis (AWE)[3] are the two primary technologies for splitting water into hydrogen and oxygen. However, both technologies suffer from sluggish oxygen evolution reaction (OER) at the anode. PEM-WE has a distinct advantage over AWE, delivering purer hydrogen at industrial current densities (1.0 A $cm^{-2}$) with superior energy conversion efficiency (70%~90%)[4,5]. Currently, commercial PEM-WEs rely on iridium (Ir) catalysts, which cost approximately USD 160,500 per kg[6], to support acidic OER owing to their notable electrochemical stability and activity under harsh acidic conditions[7,8]. The high cost of Ir catalysts restricts the global use of PEM-WE technology. Ruthenium (Ru) with a greater abundance in earth and a lower cost of USD 9523 per kg[6] is a promising alternative to partially replace Ir. Meanwhile, $RuO_2$ demonstrates higher activity than $IrO_2$ in acidic OER[9,10]. However, $RuO_2$ suffers from overoxidation during acidic OER, leading to the formation of water soluble $RuO_4$ and subsequent corrosion[11,12]. To address this, current research has focused on balancing electrochemical stability, reactivity, and cost of acidic catalyst.

---

[1] Institute of Biomedical Engineering, College of Life Sciences, Qingdao University, Qingdao, China. [2] Jiangsu Key Laboratory for Nanotechnology and Collaborative Innovation Center of Advanced Microstructures, National Laboratory of Solid State Microstructures, Nanjing University, Nanjing, China. [3] These authors contributed equally: Yanfeng Shi, Lupeng Wang, Miao Liu. e-mail: lzliu@nju.edu.cn; yhxu@qdu.edu.cn

Typically, electrochemical stability and reactivity of electrocatalysts are inversely proportional. Designing electronic structures to strengthen the bonding interactions between Ru sites and their coordination environments, stronger than the redox $H_2O/O_2$ energy, can inhibit the acidic dissolution of Ru catalysts by preventing overoxidation[13–15]. However, this approach can increase the rate-limiting potential barrier by limiting the adsorption and dissociation of reactants, reducing catalytic activity. Current reports on acidic OER primarily address the thermodynamic process[16–18], overlooking the importance of spin-related orbital hybridization and charge transfer between metal sites and derivatives. In fact, the number of unpaired electrons at metal sites is not conserved as in the four-electron OER process, which provides a feasible strategy to simultaneously optimize stability and reactivity from the viewpoint of spin catalysis[19–22]. In other words, controllable spin splitting at the Fermi level can regulate orbital degeneracy. In this case, spin-up bands with metallic characteristics can provide sufficient valence electrons to ensure catalytic activity, while spin-down bands with semiconducting characteristics can enter the bonding levels to prevent deleterious overoxidation (Supplementary Fig. 1).

Developing a suitable synthesis strategy for assembling spin-dependent catalysts is crucial to validating this proposal. Existing microstructural strategies for Ru catalysts such as doping, alloying, and amorphization[23–25] partially improve acidic OER activity but fail to deliver satisfactory overall performance. Key issues include: (1) The spin configuration of metal sites, formulated based on the lowest energy principle, cannot be easily rearranged by conventional synthesis methods[26–29]. (2) While the random anchoring of Ru patterns onto catalyst surfaces can partially enhance the atomic utilization, their bonding interactions and orbital hybridization with the matrixes become uncontrollable[30,31], and some unstable Ru particles are readily dissociated into acidic electrolytes[32]. (3) Controlling Ru atomic distribution and diffusivity at catalyst surfaces is challenging with traditional strategies, which may unintentionally undervalue the contributions of spin-relevant symmetry breaking and orbital degeneracy[33,34]. Overall, these traditional synthesis and assembly strategies for Ru catalysts cannot be separated from the solution conditions, which inspires us to implant an external microwave disturbance to timely modulate the Ru atomic bonding process. These findings can principally overcome the current technical bottlenecks. However, the microwave-mediated spin domain inversion and orbital splitting at Ru catalysts for acidic OER have yet to be addressed.

Based on the aforementioned considerations, we intentionally introduce some Cr atoms into $MnO_2$ hosts ($Mn_{1-x}Cr_xO_2$) as anchor sites, followed by a microwave-mediated cation-exchange reaction in $RuCl_3$ solution to control Ru atomic assembly ($Ru_{MW}$-$Mn_{1-x}Cr_xO_2$). This synthesis strategy offers several advantages: (1) Doped Cr atoms intentionally weaken the bonding strength of neighboring Mn–O bonds, facilitating orderly cation replacements by Ru atoms. Microwave stimulations decrease the formation probability of larger Ru particles, improving electrochemical stability and Ru atomic utilization, thereby reducing the catalyst cost. (2) Assembled Ru atoms coordinated by asymmetric Mn–O and Cr–O bonds change their orbital degeneracy and spin electron occupation, leading to a stronger bonding interaction than the redox energy of $H_2O/O_2$, thereby enhancing their stability. (3) The coherent energy superposition from microwave-mediated molecular frictions selectively assembles hydrated Ru ions and induces symmetry-breaking-dependent spin rearrangement, improving acidic OER activity. As a result, the intrinsic OER activity of $Ru_{MW}$-$Mn_{1-x}Cr_xO_2$ is two orders of magnitude higher than that of the typical heating-assembled Ru catalyst ($Ru_T$-$Mn_{1-x}Cr_xO_2$). As a proof of concept, an integrated PEM electrolyzer with the $Ru_{MW}$-$Mn_{1-x}Cr_xO_2$ catalyst achieved an industrial OER current density of $1.0\ A\ cm^{-2}$ at 1.88 V cell voltage, substantially surpassing commercial $RuO_2$ (com-$RuO_2$) catalysts ($2.49\ V@1.0\ A\ cm^{-2}$). Moreover, the technique achieves superior electricity-to-hydrogen energy conversion efficiency (88.7%), stable operation (>300 h, $1.0\ A\ cm^{-2}$), and a lower cost per gallon of gasoline equivalent for the produced $H_2$ (USD 0.87), suggesting that this approach holds immense potential for improving the hydrogen economy and reforming the energy landscape.

## Results

### Catalyst design

Generally, the four-electron OER process mainly involves intermediates such as *OH, *O, *OOH, and *OO, whose reactivities are highly dependent on the electron occupation at half-filled $d$ orbitals[35]. For reactant chemisorption, the metal active sites should have empty $t_{2g}$ orbitals to hybridize with the σ orbitals of *OH, determining the initiation of OER and accepting unpaired valence electrons. Meanwhile, separate $d$ electrons can be easily donated to the antibonding orbitals between metal sites and adsorbed *OOH species, influencing the final rate-limiting potential barrier. The electron “acceptance-donation” process between metal sites and adsorbed derivatives is crucial in determining OER performance, and this charge transfer is strongly related to electron occupation and orbital splitting[36,37]. The octahedral $RuO_6$ configuration (left panel of Fig. 1a) splits into higher $e_g$ ($d_{x^2-y^2}$ and $d_{z^2}$) and lower $t_{2g}$ ($d_{xy}$, $d_{xz}$, and $d_{yz}$) orbitals, with energy splitting and electron occupation proportional to the electronegativity differences. In this case, the symmetrical coordination of Ru sites with six oxygen atoms increases crystal field contribution but decreases intra-atomic Coulomb interactions for orbital nondegeneracy (Supplementary Figs. 2 and 3). When partially replacing Mn sites in $MnO_2$ with Ru atoms (middle panel of Fig. 1a) breaks regional symmetry, degenerating the $t_{2g}$ orbital into completely occupied $e_g$ and empty $a_{1g}$ orbitals. Adding spin-differentiating Cr atoms further breaks crystal symmetry, increasing intra-atomic Coulomb interactions (right panel of Fig. 1a). Cr doping reduces the theoretical formation energy for Ru to replace Mn sites from 2.41 to 1.92 eV, weakening Mn–O bonds at nearby Cr sites through spin-related symmetry breaking and orbital hybridization, while the higher formation energy for Ru to replace Cr sites (2.28 eV) compared to Mn sites (1.92 eV) suggests Ru preferentially substitutes Mn over Cr. The orbital degeneration induced by Jahn–Teller distortions in Ru-$Mn_{1-x}Cr_xO_2$ decreases the orbital splitting energy and helps electrons hop onto $a_{1g}$ orbitals from $e_g$ orbitals via electron–phonon interactions (Supplementary Fig. 4), and this half-filled electron occupation leads to feasible catalytic activity and stability (Supplementary Fig. 1).

The microwave modulation operating principle on cation-exchange reactions in $RuCl_3$ solution is schematically shown in Fig. 1b. Water molecules have a typical polar feature. The electric dipole interaction among water molecules will cause a molecular configuration with hydrated Ru-ionic statues that are dynamic combinations using hydrogen bonding interactions[38,39], which can be probed in subsequent Raman spectra of ionic solutions. The water molecule will bring tropism polarity under microwave stimulation, while the rotations and collisions of the water molecule will enforce the phonon vibrations of the H–O–H bond[40,41]. Infrared thermal imaging and theoretical simulation results show that this specific resonance mode’s energy superposition rapidly increases the solution temperature (Supplementary Figs. 5–7). Subsequently, coherent energies (~400–450 meV) are spontaneously injected into hydrated Ru ions via Förster energy transfer[42], making Ru ions replace Mn sites efficiently for electronic reconstruction. This microwave-triggered electron–phonon coupling uniformly activates each hydrated Ru-ion complex, inhibiting random agglomerations on $Ru_T$-$Mn_{1-x}Cr_xO_2$ catalyst surfaces (Supplementary Fig. 8). Moreover, this operation must also consider the interface coherence between the aqueous solution and the exchange substrate, which depends on their dielectric loss tangent (tan δ) values. When the exchange substrate’s tan δ value is

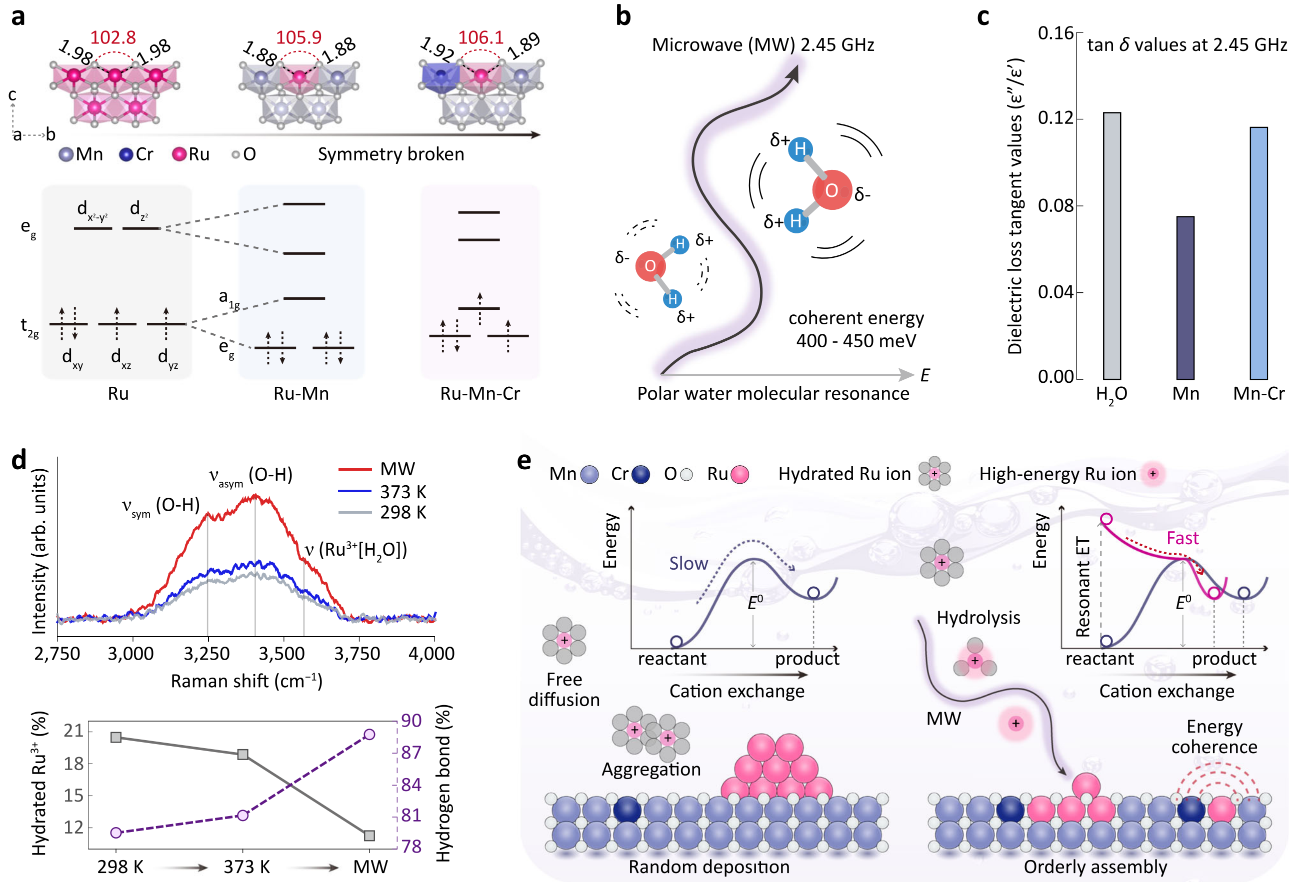

**Fig. 1 | The de novo design of reaction mechanism and catalyst. a** Top: Symmetry breaking of $RuO_6$ coordination polyhedron in the $MnO_2$ substrate mediated by Cr doping. Bottom: Splitting of the Ru 4*d* orbital for different symmetries. **b** Schematic diagram of 2.45 GHz microwave-mediated resonance of polar water molecules. **c** Comparison of dielectric loss tangent values of $MnO_2$ and $Mn_{1-x}Cr_xO_2$ substrates with water molecules. **d** Top: Raman measurements of the OH stretching vibration of $RuCl_3$ aqueous solution at different energy modes. Bottom: Proportion of deconvolution Raman peak areas for hydrogen bond and hydrated $Ru^{3+}$ species vibration under different energy modes. **e** Microwave-mediated coherent energy transfer (ET) and selective assembly of hydrated Ru ions on the $Mn_{1-x}Cr_xO_2$ substrate. arb. units, arbitrary units; ε″ and ε′, imaginary and real parts of the dielectric constant.

comparable to that of water molecules, a more available coherent energy superposition can be induced[43–45], facilitating the Ru-atomic implantation and then enhancing OER performance. Interestingly, the tan δ value of the exchange substrate can be regulated by the type and concentration of dopants, especially for Cr (Supplementary Fig. 9). The tan δ value of optimal $Mn_{1-x}Cr_xO_2$ is similar to that in water molecules but higher than pristine $MnO_2$ (Fig. 1c). The relevant radar cross-section simulations in Supplementary Fig. 10 also indicate that $Mn_{1-x}Cr_xO_2$ has a more sensitive microwave response than pristine $MnO_2$. Thus, $Mn_{1-x}Cr_xO_2$ provides better Ru assembly than pristine $MnO_2$ under microwave modulation, which can enhance the electron-phonon coupling strength through effective coherent energy superposition.

Raman spectra of $RuCl_3$ solution under traditional and microwave heating were compared (top panel of Fig. 1d). The Raman signals can be attributed to the symmetrical and asymmetrical OH stretching vibrations of water molecules and hydrated Ru ions[46–48]. The high concentration of Ru ions has a stronger hydration state and lower water activity, as indicated by the monotonous decrease in the intensity of Raman signals related to hydrogen bond interactions (Supplementary Fig. 11). Compared to traditional heating (blue line), the Raman signals were substantially enhanced with microwave modulations. The energy superposition from microwave-driven rotations and collisions makes the energetic OH-stretching strength further deviate from equilibrium position, and this noticeable change in response to the structural force constants in the excited state can be intuitively reflected by the Raman fingerprints. The deconvolution of Raman peak areas for hydrogen bonds and hydrated Ru ion species (Supplementary Fig. 12 and Table 1) and comparison (bottom panel of Fig. 1d) clarify their intrinsic differences. The OH stretching vibrations are substantially enhanced under microwave heating compared to traditional heating. Conversely, the proportion of hydrated Ru-ion species decreases due to microwave-induced energy transfer, facilitating Ru atom diffusivity by breaking the hydrated bonds.

To better understand the specific assembly of Ru patterns, the microwave-mediated cation-exchange reaction at $Mn_{1-x}Cr_xO_2$ surfaces in $RuCl_3$ solution is schematically shown in Fig. 1e. Theoretically, the traditional cation-exchange reaction must overcome a minimum potential barrier of about 353 meV (Supplementary Fig. 13). The slower assembly kinetic rate leads to a longer reaction time (more than 12 h). In this process, some hydrated Ru ions may spontaneously congregate together by hydrogen bond interaction of the hydration layer and finally be adsorbed on $Mn_{1-x}Cr_xO_2$ surfaces as unstable Ru particles. If molecular phonon vibration energies are coherently transferred into hydrated Ru ions via Förster energy transfer under microwave stimulation, the relative potential barrier for cation-exchange reactions will be transiently diminished, making the substitution of Ru atoms easier (less than 30 min). Experimentally, the relevant energy superposition process and the minimum energy required for the optimal Ru atomic assembly were revealed by further modulating the microwave time and power (Supplementary Figs. 14 and 15).

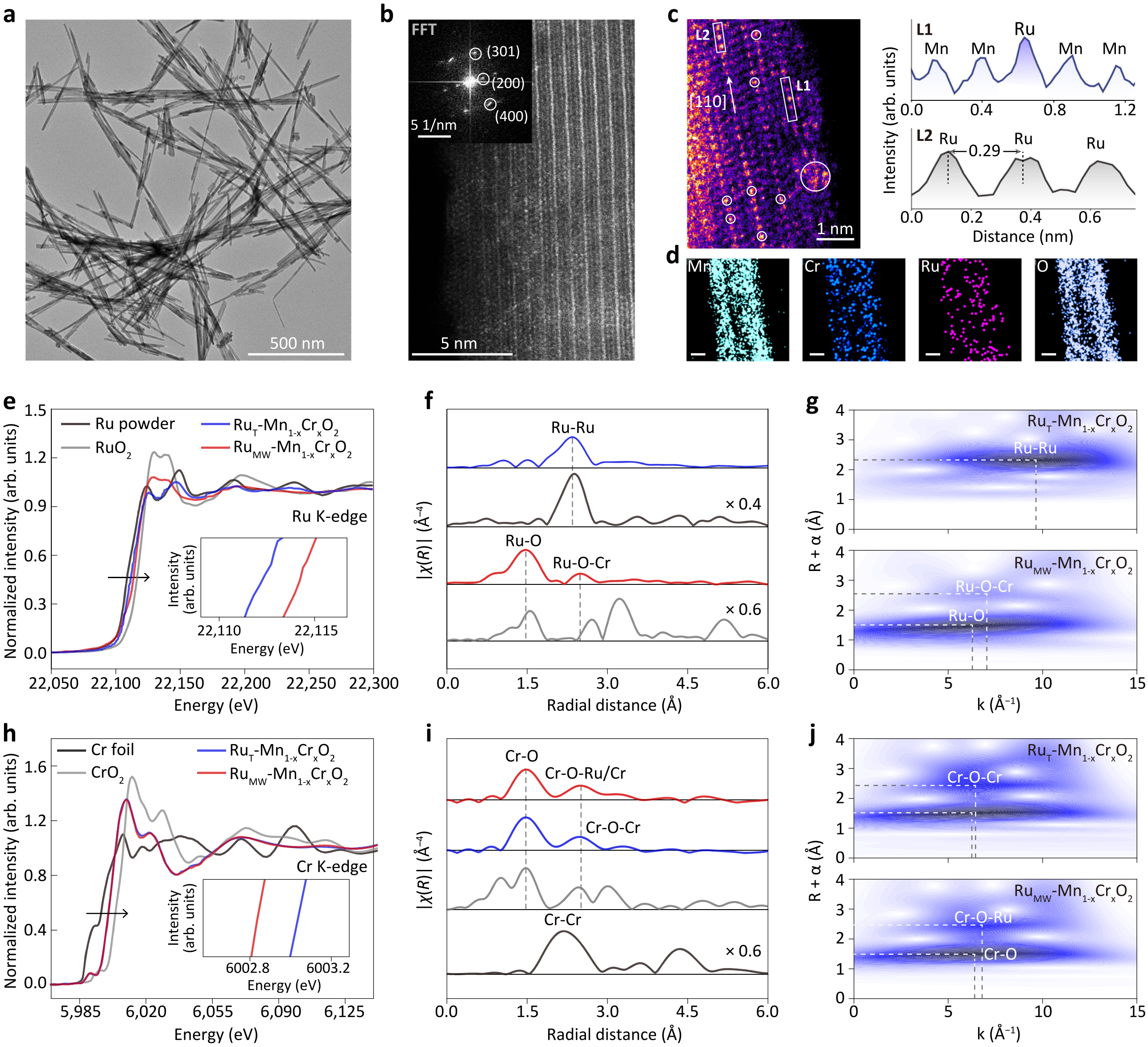

**Fig. 2 | Morphology and structural characterizations of electrocatalysts. a** TEM image of the Ru$_{MW}$-Mn$_{1-x}$Cr$_x$O$_2$ catalyst, showing nanowire morphology similar to that of α-MnO$_2$ and reference samples. **b** Aberration-corrected HAADF-STEM image of Ru$_{MW}$-Mn$_{1-x}$Cr$_x$O$_2$ at low magnification. Inset: Electron diffraction image obtained by fast Fourier transform (FFT). **c** Aberration-corrected HAADF-STEM image of Ru$_{MW}$-Mn$_{1-x}$Cr$_x$O$_2$ at high magnification. Insets on the right show the corresponding intensity profiles labeled with L1 and L2 boxes. **d** Corresponding EDS mappings of Ru$_{MW}$-Mn$_{1-x}$Cr$_x$O$_2$. The scale bar represents 1 nm. Normalized Ru K-edge XANES (**e**) and k$^3$-weighted Fourier transform EXAFS (**f**) spectra for Ru$_T$-Mn$_{1-x}$Cr$_x$O$_2$ (blue line) and Ru$_{MW}$-Mn$_{1-x}$Cr$_x$O$_2$ (red line). **g** Wavelet transform EXAFS of the Ru K-edge for Ru$_T$-Mn$_{1-x}$Cr$_x$O$_2$ (top) and Ru$_{MW}$-Mn$_{1-x}$Cr$_x$O$_2$ (bottom). Normalized Cr K-edge XANES (**h**) and k$^3$-weighted Fourier transform EXAFS (**i**) spectra for Ru$_T$-Mn$_{1-x}$Cr$_x$O$_2$ (blue line) and Ru$_{MW}$-Mn$_{1-x}$Cr$_x$O$_2$ (red line). **j** Wavelet transform EXAFS of the Cr K-edge for Ru$_T$-Mn$_{1-x}$Cr$_x$O$_2$ (top) and Ru$_{MW}$-Mn$_{1-x}$Cr$_x$O$_2$ (bottom). arb. units, arbitrary units; **k**, wave vector.

## Structural characterization of catalysts

A series of structural characterizations confirm the Ru$_{MW}$-Mn$_{1-x}$Cr$_x$O$_2$ proposal. Transmission electron microscopy (TEM) images (Fig. 2a) show that the nanofiber morphology of Ru$_{MW}$-Mn$_{1-x}$Cr$_x$O$_2$ remained unchanged compared to pristine Mn$_{1-x}$Cr$_x$O$_2$ and other samples (Supplementary Fig. 16). Aberration-corrected high-angle annular dark-field scanning transmission electron microscopy (HAADF-STEM) images (Fig. 2b) show that the Ru atoms are brighter than neighboring Mn and Cr atoms owing to their significant mass difference. The fast Fourier transform images of Ru$_{MW}$-Mn$_{1-x}$Cr$_x$O$_2$ in the inset of Fig. 2b reveal good crystal structure with typical (301), (200), and (400) planes; slight lattice distortion can be observed comparing with the Mn$_{1-x}$Cr$_x$O$_2$ host (Supplementary Fig. 17). Microwave-activated Ru atoms are successfully implanted onto Mn$_{1-x}$Cr$_x$O$_2$ surfaces, primarily as single-atom sites or regular Ru atomic chains with a Ru–Ru interatomic distance of 2.91 Å (Fig. 2c). Although some sub-nanometer Ru clusters are detected, substantially different from massive Ru particles in traditional cation-exchange reactions (Supplementary Fig. 18). This microwave-mediated assembly pattern enhances Ru species' utilization and stability. Peak fitting and Rietveld refinement analysis of powder X-ray diffraction patterns demonstrate a well-ordered I4/m symmetry, but differences in Ru atomic assembly cause some peak broadening (Supplementary Fig. 19 and Table 2). It can be easily understood that the implantation of Ru atoms into Mn$_{1-x}$Cr$_x$O$_2$ could lead to localized structural distortion more readily than simply random deposition without microwave modulation, and the symmetry-breaking-dependent structure factor causes some slight differences in XRD and Raman fingerprints (Supplementary Fig. 20)[49,50]. Element mappings (Fig. 2d) indicate the coexistence of Mn, Cr, Ru, and O elements in the $Ru_{MW}$-$Mn_{1-x}Cr_xO_2$ sample, and the corresponding energy-dispersive spectrum (EDS) was provided (Supplementary Fig. 21 and Table 3). The element contents of different samples were further determined via inductively coupled plasma optical emission spectroscopy (ICP-OES), as detailed in Supplementary Table 4. It is observed that Mn content decreases with some Ru atoms being selectively implanted, while Cr content remains virtually unchanged. Based on the above ICP results and the Pauli electronegativity principle, we can conclude that Ru atoms prefer to occupy the Mn sites, which can be further elucidated by X-ray photoelectron spectroscopy (XPS) analysis (Supplementary Fig. 22).

Ru atomic configurations and their interatomic interactions were studied using X-ray absorption spectroscopy. The Ru K-edge X-ray absorption near-edge structure (XANES) spectra and amplified absorption pre-edge shifts (the insert of Fig. 2e) indicate that the Ru species' oxidation state in $Ru_{MW}$-$Mn_{1-x}Cr_xO_2$ is higher than that in $Ru_T$-$Mn_{1-x}Cr_xO_2$, with an average positive valence between Ru powder (0) and $RuO_2$ (+4), consistent with XPS analysis (Supplementary Fig. 23). The difference in Ru oxide state can be attributed to the microwave-mediated orderly Ru atomic assembly and electronic interaction of the neighboring lattice Cr sites[51]. The extended X-ray absorption fine-structure (EXAFS) spectrum of $Ru_{MW}$-$Mn_{1-x}Cr_xO_2$ shows a prominent scattering path at ~1.48 Å and a weaker second-shell signal at ~2.51 Å (Fig. 2f), corresponding to the Ru−O and Ru−O−Cr units, respectively. In contrast, an obvious peak appears at ~2.35 Å in both $Ru_T$-$Mn_{1-x}Cr_xO_2$ and Ru powder, which can be assigned to the metallic Ru−Ru coordination. The least-squares EXAFS curve fitting was conducted to further extract the fine configuration of Ru atomic assembly (Supplementary Fig. 24 and Table 5). Notably, the Ru−O coordination of $Ru_{MW}$-$Mn_{1-x}Cr_xO_2$ displays a shorter radial distance (R) and a lower centrosymmetry degree compared to $RuO_2$, which may originate from the contribution of local lattice distortion induced by the Ru−O−Cr configuration with symmetry breaking[52]. These results reveal that microwave-mediated coherent energy superposition facilitates orderly Ru atomic assembly and reduces the formation probability of Ru particles, which is observed in the Morlet wavelet transform (WT) more clearly (Fig. 2g). More discussions regarding the structure differences of the Ru assembly were provided in Supplementary Fig. 25. To further elucidate the interaction between Ru and Cr sites, Cr K-edge XANES and EXAFS spectra were also conducted. The average Cr oxidation state in $Ru_{MW}$-$Mn_{1-x}Cr_xO_2$ is slightly lower than that of $Ru_T$-$Mn_{1-x}Cr_xO_2$, as indicated by the energy position of absorption pre-edges (Fig. 2h) and relevant XPS analysis (Supplementary Fig. 26). This suggests potential bonding interactions and charge transfer between Cr and Ru sites. The EXAFS spectra of both samples show a dominant Cr−O signal at ~1.49 Å with no Cr−Cr scattering peak, indicating atomic dispersion of Cr in the $MnO_2$ substrate (Fig. 2i). Notably, the second-shell signal in $Ru_{MW}$-$Mn_{1-x}Cr_xO_2$ exhibits a slightly positive shift compared with Cr−O−Cr in $Ru_T$-$Mn_{1-x}Cr_xO_2$, which may be related to the local Cr−O−Ru interactions[52,53]. The WT-EXAFS spectra show that (Fig. 2j) the second-shell in $Ru_{MW}$-$Mn_{1-x}Cr_xO_2$ is located at ~6.9 $Å^{-1}$ in **k** space, larger than ~6.4 $Å^{-1}$ for the Cr−O−Cr path in $Ru_T$-$Mn_{1-x}Cr_xO_2$, due to the stronger back-scattering of Ru atoms compared to neighboring Cr atoms. The differences of **k** values further corroborate the contribution of the Cr−O−Ru configuration. In a word, microwave stimulation effectively modulates the assembly pattern and local coordination environment of Ru atoms, which will further affect reactive Ru sites' spin-dependent electronic structure.

## Spin-related properties of catalysts

To display microwave-induced spin-dependent electronic reconfiguration, the magnetization of $Mn_{1-x}Cr_xO_2$ as a function of magnetic field (M-H) with different assembly strategies was compared using a superconducting quantum interference device (SQUID) at room temperature (Fig. 3a). For pristine $Mn_{1-x}Cr_xO_2$ sample, the M-H loop is linear without remanent magnetization, indicating paramagnetic behavior. The magnetic domains are randomly distributed due to room-temperature thermal disturbance (low spin: LS). When Ru patterns are selectively assembled onto $Mn_{1-x}Cr_xO_2$ surfaces, the slope of M-H loop decreases, especially in the $Ru_{MW}$-$Mn_{1-x}Cr_xO_2$ sample. Compared with random Ru particle deposition on $Ru_T$-$Mn_{1-x}Cr_xO_2$, the bonding interaction and orbital hybridization in $Ru_{MW}$-$Mn_{1-x}Cr_xO_2$ will be changed as symmetry breaking induced by selective Ru-atomic implantation. The corresponding multistage orbital degeneracy causes a spin domain flipping to a certain extent (the insert of Fig. 3a), leading to a more ordered spin configuration (high spin: HS) and distinguishable magnetic structure. Notably, the unchanged magnetic susceptibility of $MnO_2$-based samples shows the critical role of Cr incorporation in modulating spin structures (Supplementary Fig. 27). According to Heisenberg model[54], the energy difference between HS and LS configurations can be quantitatively expressed as follows: $\Delta E = E_{LS} - E_{HS} = \sum_{ij} J_{ij} S_i \cdot S_j$, where $J_{ij}$ is the spin-exchange interaction strength, and $S_i$ and $S_j$ are the magnetic moments at the spin nets. The calculations show that HS configuration is more stable than LS configuration ($\Delta E$ is ~0.363 eV). The paramagnetic response difference shows that the orderly Ru atomic assembly at $Ru_{MW}$-$Mn_{1-x}Cr_xO_2$ can also lead to a spin-related electronic reconfiguration, as confirmed by the temperature-dependent magnetization (M-T) curves (Fig. 3b). Generally, the relative magnetization intensity decreases with increasing temperature, but a cross point between $Ru_{MW}$-$Mn_{1-x}Cr_xO_2$ and $Ru_T$-$Mn_{1-x}Cr_xO_2$ was observed at ~350 K, indicating a stronger spin-exchange interaction induced by spin-flop transition.

The electron energy loss spectroscopy (EELS) was performed to determine the spin-dependent electronic reconfigurations (Fig. 3c and Supplementary Fig. 28). Typically, the fingerprint feature of Ru M-edge is primarily determined by the structural symmetry and spin electron occupation[55]. The partial replacement in $Ru_{MW}$-$Mn_{1-x}Cr_xO_2$ makes some electrons of Ru donate to the nearby Cr sites and a larger Ru-*d* half-filled electron density will increase the $M_3$ intensity. The integral peak area ratio ($I_w$) between the Ru M-edges after removing the baselines ($I_w = M_3/(M_2 + M_3)$) was calculated to gain insights into the Ru spin-state. Compared with the $Ru_{MW}$-$MnO_2$ and $Ru_T$-$Mn_{1-x}Cr_xO_2$, the $I_w$ value of $Ru_{MW}$-$Mn_{1-x}Cr_xO_2$ sample increased, while the peak position blue-shifted to the high-energy region, corresponding to HS configuration. This is because the multistage orbital hybridizations induced by the microwave-mediated symmetry-breaking-dependent Ru-atomic patterns can facilitate valence electron hopping from the $e_g$ orbital to the $a_{1g}$ orbital, leading to a spin-electronic reoccupation.

Spin-resolved projected density of state (PDOS) of Ru sites was determined to comprehend spin-dependent electron occupation (Fig. 3d). Based on the Goodenough−Kanamori rule[56], the spin-exchange interaction between two neighboring $t_{2g}$ orbitals will give rise to antiferromagnetic (AFM) behavior. When electrons at the lower $t_{2g}$ orbital are easily hopped onto a higher half-filled $a_{1g}$ orbital, the strong spin-exchange interaction will lead to a conversion from AFM to ferromagnetic (FM) behavior. Therefore, the electronic occupation at the Fermi level plays a crucial role in triggering a spin-flop transition. For the Ru-$MnO_2$ configuration, no obvious spin-polarized electrons populate at the Fermi level. Conversely, the Fermi level of Ru-$Mn_{1-x}Cr_xO_2$ is fully occupied by the spin-up state, in which some electrons can be energetically exchanged between $t_{2g}$ and $a_{1g}$ orbitals. This is why the spin-flop transition preferentially occurs in the Ru-$Mn_{1-x}Cr_xO_2$ configuration.

The spin-flop transition from LS to HS configuration is generally accompanied by changing the unpaired electrons. To further unveil their spin-dependent electron transition, the electron spin resonance (ESR) spectra of different samples were compared at room temperature (Fig. 3e). A distinguishable peak at $g = 2.00$ was observed for $Ru_{MW}$-$Mn_{1-x}Cr_xO_2$ sample that corresponds with a partial spin-flop

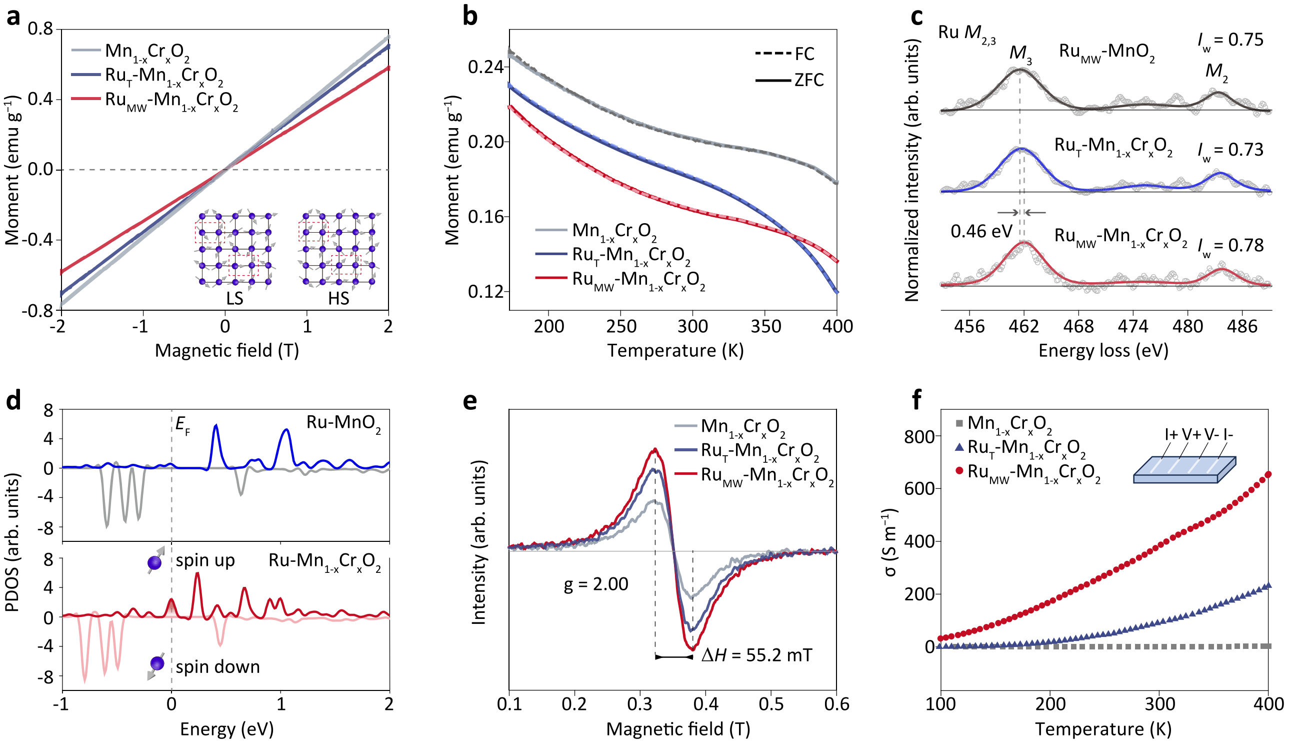

**Fig. 3 | Characterization of spin-related magnetic and electronic properties.** **a** Room-temperature magnetic hysteresis loops of $Mn_{1-x}Cr_xO_2$, $Ru_T$-$Mn_{1-x}Cr_xO_2$, and $Ru_{MW}$-$Mn_{1-x}Cr_xO_2$. Insets show magnetic ordering patterns in low-spin (LS) and high-spin (HS) states. **b** ZFC (zero field-cooled) and FC (field-cooled) magnetization curves of $Mn_{1-x}Cr_xO_2$, $Ru_T$-$Mn_{1-x}Cr_xO_2$, and $Ru_{MW}$-$Mn_{1-x}Cr_xO_2$ as a function of temperature with a 5000 Oe external magnetic field. **c** EELS spectra of the Ru M-edge for $Ru_{MW}$-$MnO_2$, $Ru_T$-$Mn_{1-x}Cr_xO_2$, and $Ru_{MW}$-$Mn_{1-x}Cr_xO_2$. **d** Spin-resolved PDOS for the Ru element in Ru-$MnO_2$ and Ru-$Mn_{1-x}Cr_xO_2$. $E_F$ represents Fermi level. **e** ESR spectra of $Mn_{1-x}Cr_xO_2$, $Ru_T$-$Mn_{1-x}Cr_xO_2$, and $Ru_{MW}$-$Mn_{1-x}Cr_xO_2$ recorded at room temperature. $\Delta H$ represents line width of the spectrum. **f** Electrical conductivity (σ) as a function of temperature for $Mn_{1-x}Cr_xO_2$, $Ru_T$-$Mn_{1-x}Cr_xO_2$, and $Ru_{MW}$-$Mn_{1-x}Cr_xO_2$. Inset: Schematic of the electrode resistance measured by the four-terminal sensing method. arb. units, arbitrary units.

transition at the HS configuration. The electron occupation at multiple half-filled *d* orbitals with HS state leads to complex Zeeman splitting and resonance energy absorption[57], broadening the region of signal response. Combining the O 1*s* XPS results from Supplementary Fig. 29, we can conclude that the primary differences in ESR signals stem from spin-state transition. As a comparison, the signal response decreased for $Ru_T$-$Mn_{1-x}Cr_xO_2$, further indicating that microwave-mediated coordinatively distorted π-donor ligands enhance the *d*-orbital degeneracy and electron pairing energy.

Temperature-related conductivity (*σ*) of different samples was measured to establish the relationship between electron–phonon couplings and microwave-mediated atomic assembly (Fig. 3f). $Ru_{MW}$-$Mn_{1-x}Cr_xO_2$ showed higher conductivity than $Mn_{1-x}Cr_xO_2$ and $Ru_T$-$Mn_{1-x}Cr_xO_2$. The conductivity linearly increases with increasing temperature owing to the thermal excitation from phonon–electron interaction, indicating semiconductor behavior. In principle, the high-energy hot carriers at $Ru_{MW}$-$Mn_{1-x}Cr_xO_2$ mainly confront lattice symmetry-breaking-induced single electron–phonon scattering (Supplementary Fig. 30). Conversely, randomly deposited Ru particles on $Ru_T$-$Mn_{1-x}Cr_xO_2$ cause multiple electron–phonon scattering as interparticle interaction can partially hinder the migration of hot carriers. The temperature-dependent conductivity differences also demonstrate the advantage of microwave-mediated Ru atomic assembly in accelerating carrier migration.

## Electrocatalytic performance

To disclose the relationship between spin-sensitive Ru atomic assembly and acidic OER activity, the linear sweep voltammetry (LSV) curves of different samples were measured in 0.1 M $HClO_4$ (Fig. 4a). All electrode potentials have been converted into the reversible hydrogen electrode (RHE). The catalytic activities of pristine $MnO_2$ and $Mn_{1-x}Cr_xO_2$ are inferior to com-$RuO_2$, indicating that superficial Mn or Cr sites cannot easily trigger an acidic OER (Supplementary Fig. 31). When Ru atoms are selectively assembled onto electrode surfaces using a microwave-mediated strategy, the reactivities can be substantially enhanced, especially for $Ru_{MW}$-$Mn_{1-x}Cr_xO_2$ sample. Cr doping in $Mn_{1-x}Cr_xO_2$ optimizes the microwave-mediated Ru atomic assembly, making $Ru_{MW}$-$Mn_{1-x}Cr_xO_2$ superior to $Ru_{MW}$-$MnO_2$. More interestingly, traditional heating-regulated Ru atomic assembly ($Ru_T$-$MnO_2$ and $Ru_T$-$Mn_{1-x}Cr_xO_2$) does not achieve ideal OER behavior (Supplementary Fig. 32) due to randomly deposited Ru particles' inability to provide half-filled *d* orbitals for optimal orbital hybridization and bonding interaction with O 2*p* orbitals of intermediates.

Specific electrochemical metrics were measured or calculated to comprehensively compare the OER performance of different samples (Fig. 4b and Supplementary Table 6). The lower overpotential and Tafel slope of $Ru_{MW}$-$Mn_{1-x}Cr_xO_2$ indicate its superior OER dynamics (Supplementary Figs. 33 and 34), including 1–3 orders of magnitude higher mass activity, specific activity, and turnover frequency than other samples (Supplementary Figs. 35–38). $Ru_{MW}$-$Mn_{1-x}Cr_xO_2$ is one of the most active electrocatalysts among the state-of-the-art Ru/Ir-based materials reported in literature (Supplementary Table 7). Moreover, $Ru_{MW}$-$Mn_{1-x}Cr_xO_2$ operated at 10 mA cm$^{-2}$ for over 200 h with a negligible increase in potential in sharp contrast to $Ru_T$-$Mn_{1-x}Cr_xO_2$ and com-$RuO_2$ (Supplementary Fig. 39). Long-term ICP measurements of Ru and Mn elements in the electrolyte show that the disparity in stability stems from the rapid dissolution of unstable Ru particles on $Ru_T$-$Mn_{1-x}Cr_xO_2$ during acidic OER (Supplementary Fig. 40). Moreover, the structural evolution, magnetic structure and electronic state transition of the catalysts during the acidic OER process were further probed by

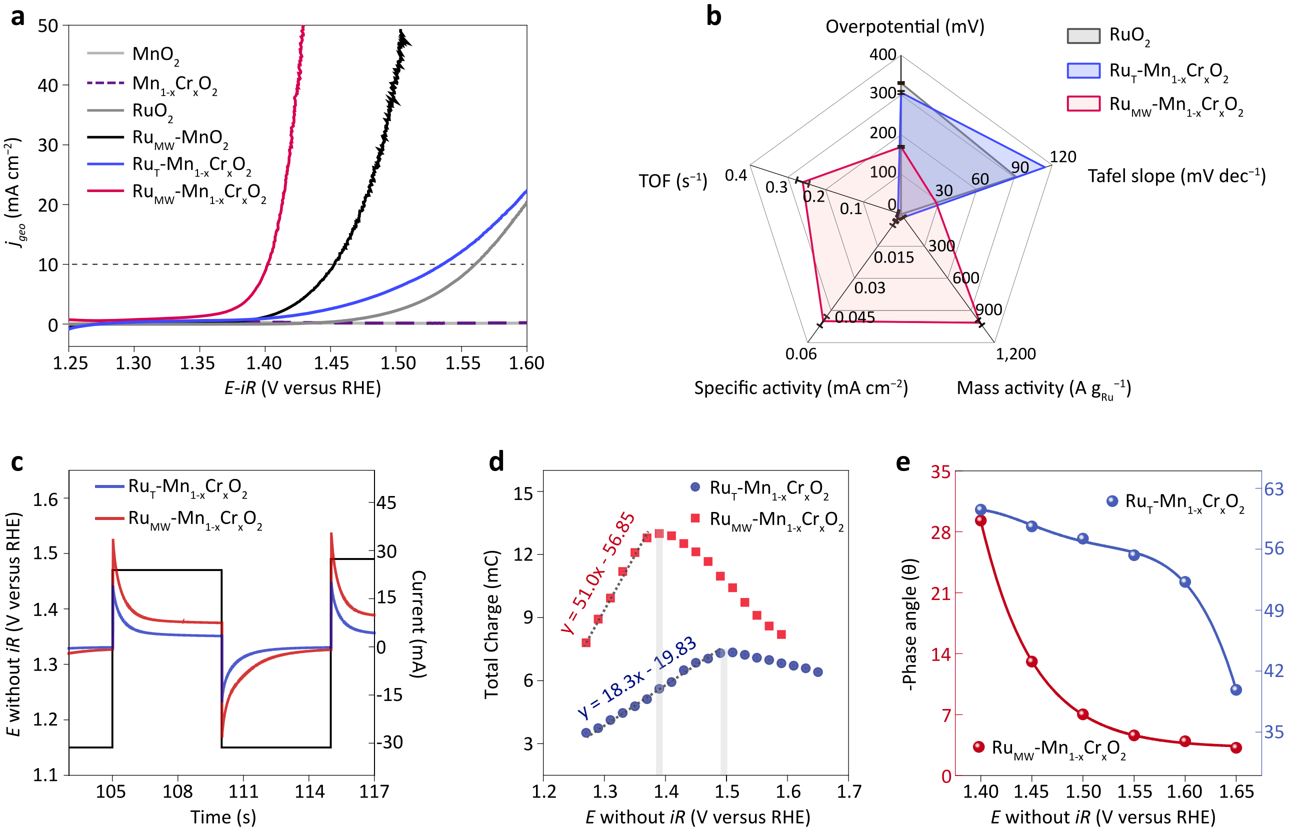

**Fig. 4 | OER performance.** **a** LSV polarization curves (*iR*-corrected) of MnO$_2$, Mn$_{1-x}$Cr$_x$O$_2$, RuO$_2$, Ru$_{MW}$-MnO$_2$, Ru$_T$-Mn$_{1-x}$Cr$_x$O$_2$, and Ru$_{MW}$-Mn$_{1-x}$Cr$_x$O$_2$ in 0.1 M HClO$_4$. The solution resistance (*R*) is about 10 ± 0.8 Ω. **b** Comparison of overpotential (10 mA cm$^{-2}$), Tafel slopes, mass activities, specific activities, and TOF at a voltage of 1.45 V vs. RHE for RuO$_2$, Ru$_T$-Mn$_{1-x}$Cr$_x$O$_2$, and Ru$_{MW}$-Mn$_{1-x}$Cr$_x$O$_2$. Data are presented as mean values ± s.d. (*n* = 3). **c** Section of the pulse voltammetry protocol (black) showing an oxidative and reductive pulses of Ru$_T$-Mn$_{1-x}$Cr$_x$O$_2$ and Ru$_{MW}$-Mn$_{1-x}$Cr$_x$O$_2$ with the current response. **d** Total charge (integral anodic charge) of Ru$_T$-Mn$_{1-x}$Cr$_x$O$_2$ and Ru$_{MW}$-Mn$_{1-x}$Cr$_x$O$_2$ versus potential from pulse voltage induced current (PVC). **e** Response of the phase angle to the applied potential of Ru$_T$-Mn$_{1-x}$Cr$_x$O$_2$ and Ru$_{MW}$-Mn$_{1-x}$Cr$_x$O$_2$. The applied potentials in **c**, **d**, and **e** were without *iR* correction.

XPS, TEM, XRD, SQUID, and in-situ Raman measurements (Supplementary Figs. 41–46). All these results indicate that the microwave-mediated Ru$_{MW}$-Mn$_{1-x}$Cr$_x$O$_2$ catalyst has superior OER activity and structural stability in acidic media.

The differences in catalytic activity can be quantitatively assessed using pulse voltammetry (PV) (Supplementary Fig. 47). The oxidation of active sites under bias in PV tests will form an oxidative charge involved in acidic OER[58]. The degree of oxidation reflects changes in the pseudo-capacitance of Ru catalysts, related to the symmetry-breaking-dependent electronic reconfiguration. Figure 4c shows the partial redox pulse currents of Ru$_T$-Mn$_{1-x}$Cr$_x$O$_2$ (blue) and Ru$_{MW}$-Mn$_{1-x}$Cr$_x$O$_2$ (red), followed by the PV protocol (black). Generally, the decay behavior in the current response of Ru$_{MW}$-Mn$_{1-x}$Cr$_x$O$_2$ is slower than that of Ru$_T$-Mn$_{1-x}$Cr$_x$O$_2$ because the multilevel orbital splitting and spin transition induced by asymmetric Ru atomic patterns provides more half-filled *d* orbitals for the electronic "acceptance-donation" process (Supplementary Fig. 48). Conversely, randomly deposited Ru particles on Ru$_T$-Mn$_{1-x}$Cr$_x$O$_2$ display metallic behavior, and the delocalization of electronic state makes the current response more sensitive. The instantaneous charge storage in different catalysts as a function of the applied voltage pulse is quantified by integrating the response currents after deducting the OER background current (Supplementary Fig. 49). The relationship between charge storage and applied potentials shows a bilinear behavior for different electrochemical process, indicating that capacitance values vary with slope (Fig. 4d). When reactants are adsorbed onto active sites and slowly become saturated, the instantaneous electronic reconfiguration compels the charge storage capacity to change with increase in potential. Compared with Ru$_T$-Mn$_{1-x}$Cr$_x$O$_2$, Ru$_{MW}$-Mn$_{1-x}$Cr$_x$O$_2$ exhibits a faster oxidative charge accumulation and dissipation behavior, lowering the OER activation energy and facilitating the deprotonation coupling electron transfer process. The difference in charge in this synchronized short-time transient as a function of log OER current (Supplementary Fig. 50) shows that oxidative charge accumulation on catalysts may directly affect the OER rate[59,60].

To further analyze the differences in reaction kinetics, in-situ electrochemical impedance spectroscopy (EIS) tests were performed at various applied biases. Ru$_{MW}$-Mn$_{1-x}$Cr$_x$O$_2$ exhibited an accelerating trend of phase angle decline at low-frequency regions, indicating that the charge transfer between catalyst surfaces and electrolyte is substantially enhanced due to microwave-mediated spin-sensitive Ru atomic assembly (Fig. 4e and Supplementary Fig. 51). Meanwhile, the carrier migration in Ru$_{MW}$-Mn$_{1-x}$Cr$_x$O$_2$ becomes easier than in Ru$_T$-Mn$_{1-x}$Cr$_x$O$_2$ (Supplementary Fig. 52) because the multiple electronic scattering from random Ru interparticles can be avoided. The lower charge transfer resistance of Ru$_{MW}$-Mn$_{1-x}$Cr$_x$O$_2$ facilitates the adsorption and activation of oxygen-containing species, leading to faster reaction kinetics for acidic OER applications.

## Insights into OER mechanism

The reaction mechanism of acidic OER was elucidated from in-situ attenuated total reflectance surface-enhanced infrared absorption spectroscopy (ATR-SEIRAS) (Fig. 5a and Supplementary Fig. 53) owing to its sensitivity to dynamic surface reconstitution with adsorbed intermediates. The intrinsic ATR-SEIRAS signals of Ru$_{MW}$-Mn$_{1-x}$Cr$_x$O$_2$

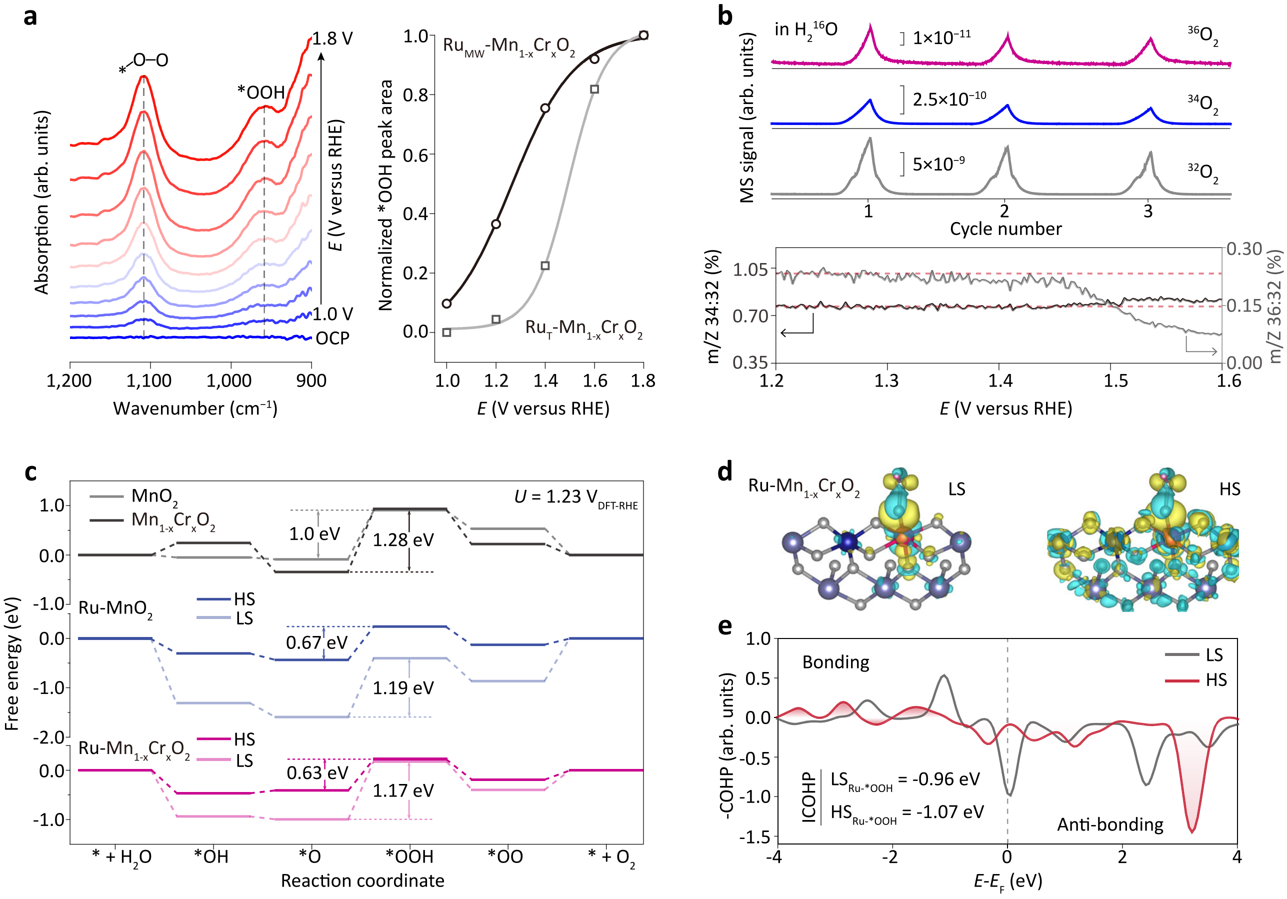

**Fig. 5 | In-situ characterization and spin configuration-tuned OER mechanism.** **a** Left: In-situ ATR-SEIRAS measurements in the range of 900–1200 cm$^{-1}$ at various applied potentials vs. RHE for $Ru_{MW}$-$Mn_{1-x}Cr_xO_2$. Right: Potential-dependent normalized *OOH peak areas of $Ru_T$-$Mn_{1-x}Cr_xO_2$ (grey line) and $Ru_{MW}$-$Mn_{1-x}Cr_xO_2$ (black line). **b** Top: DEMS signals of $O_2$ products for $Ru_{MW}$-$Mn_{1-x}Cr_xO_2$ in the electrolyte using $H_2{}^{16}O$ as the solvent during three cycles of LSV in the potential range of 1.1–1.75 V vs. RHE, with a scan rate of 5 mV s$^{-1}$. Bottom: The $^{34}O_2$:$^{32}O_2$ and $^{36}O_2$:$^{32}O_2$ signal ratios of $Ru_{MW}$-$Mn_{1-x}Cr_xO_2$ during the OER process with $H_2{}^{16}O$ as the electrolyte solvent. **c** Computed free energies of intermediates for the AEM-type OER at different reactive sites and spin states. $U = 1.23$ V vs. RHE. Charge density difference (**d**) and relative COHP of adsorbed *OOH (**e**) onto the Ru site at $Ru_{MW}$-$Mn_{1-x}Cr_xO_2$ with LS and HS states. The yellow regions in **d** show charge depletion, while the blue regions show charge accumulation. MS mass spectrometry, arb. units, arbitrary units, LS low spin, HS high spin, $E_F$ fermi level.

sample merged with increasing potential (1.0–1.8 V vs. RHE), while oxygen bubbles slowly appeared at the electrodes. The intensity of two distinct adsorption bands at 960 cm$^{-1}$ and 1108 cm$^{-1}$ substantially increased with potential exceeding the OER region potential (≥1.3 V). This can be attributed to the formation of surface-adsorbed *OOH and linearly bonded superoxol species (*OO)[61], where *OOH is a typical intermediate for adsorbate-evolving mechanism (AEM) (Supplementary Fig. 54). Moreover, the $Ru_T$-$Mn_{1-x}Cr_xO_2$ sample exhibited similar FTIR signals, suggesting the same AEM pathway as $Ru_{MW}$-$Mn_{1-x}Cr_xO_2$. However, the weaker intensity and higher threshold potential observed indicate slower OER kinetics (Supplementary Fig. 55). Owing to this distinctive FTIR signal response, their catalytic properties were quantitatively evaluated by calculating the relative peak area ($R_A$) of intermediates as follows: $R_A = \int I_E / \int I_{max}$, where $I_E$ is the peak intensity of *OOH intermediate at different applied potentials and $I_{max}$ is the maximum value of $I_E$. The normalized peak areas of *OOH in $Ru_T$-$Mn_{1-x}Cr_xO_2$ and $Ru_{MW}$-$Mn_{1-x}Cr_xO_2$ with varying potential were compared (right panel of Fig. 5a). The signal area of $Ru_{MW}$-$Mn_{1-x}Cr_xO_2$ with intermediates rapidly increased at ~1.35 V and then slowly reached a maximum value, demonstrating a typical OER process. However, the relative signal area of $Ru_T$-$Mn_{1-x}Cr_xO_2$ is less than that of $Ru_{MW}$-$Mn_{1-x}Cr_xO_2$, and the potential for initiating OER blue-shifted to 1.45 V. This ATR-SEIRAS signal response between $Ru_{MW}$-$Mn_{1-x}Cr_xO_2$ and $Ru_T$-$Mn_{1-x}Cr_xO_2$ reveals their differences in reaction kinetics during acidic OER.

To further monitor the acidic OER behaviors, in-situ differential electrochemical mass spectrometry (DEMS) measurements were performed using the isotope $^{18}O$-labeling method (Supplementary Fig. 56). $Ru_{MW}$-$Mn_{1-x}Cr_xO_2$ was first labeled with $^{18}O$ by performing LSV cycles in $H_2{}^{18}O$ electrolyte (Supplementary Fig. 57a). The relative XPS measurement shows that abundant $^{16}O$ species spontaneously adsorbed onto the catalyst surface (before $^{18}O$-labeling operation) (Supplementary Fig. 29)[61]. Therefore, the corresponding $^{32}O_2$ ($^{16}O + {}^{16}O$), $^{34}O_2$ ($^{16}O + {}^{18}O$), and $^{36}O_2$ ($^{18}O + {}^{18}O$) species were formed from $H_2{}^{18}O$ and intrinsic $^{16}O$ species through AEM pathway, with $^{36}O_2$ being the dominant product along with trace amounts of $^{34}O_2$ and $^{32}O_2$ for each OER cycle. Distinct signals of these gaseous products indicate that the catalyst surfaces are labeled with large amounts of $^{18}O$ if the acidic OER process is promoted by lattice oxygen mechanism (LOM). The labeled catalyst was thoroughly washed with abundant deionized water, and the DEMS measurements for OER cycles in $H_2{}^{16}O$ electrolyte were repeated (top panel of Fig. 5b). The signal response of $^{32}O_2$ is obviously higher than that of $^{34}O_2$ and $^{36}O_2$. And the corresponding MS signals as a function of potentials (Supplementary Fig. 57b) show a typical initiation behavior of AEM-type OER. $Ru_T$-$Mn_{1-x}Cr_xO_2$ sample showed similar signal distributions, but with magnitude differences (Supplementary Fig. 58). More importantly, the relative signal ratio of $^{34}O_2$:$^{32}O_2$ (black line) within the OER working windows (1.2–1.6 V vs. RHE) hardly unchanged (bottom panel of Fig. 5b) and is comparable to that of the abundance of $^{18}O$ in natural water or residual $^{18}O$ adsorbates at the previous step within experimental uncertainty[62], indicating that the LOM cannot happen over $Ru_{MW}$-MmCrO$_2$. Meanwhile, the relative signal ratio of $^{36}O_2$: $^{32}O_2$ (gray line) gradually decreased with increasing potential, further confirming the dominance of AEM pathway during acidic OER[63].

Comprehensive comparison of free energies for each intermediate in the AEM pathway (Fig. 5c and Supplementary Fig. 59) were conducted to reveal the correlation between reactivity and microwave-mediated symmetry-breaking-dependent spin electronic reconfiguration. The relative difference in free energy between successive derivatives plays a crucial role in determining the activation energy at rate-limiting steps. For pristine $MnO_2$ surface, the rate-determining intermediate originates from the generation of *OOH (top panel), requiring additional energy of 1.0 eV to continue follow-up reactions. When Cr atoms are doped into $MnO_2$ surface to construct $Mn_{1-x}Cr_xO_2$ slab, the potential barrier with the formed *OOH increases to 1.28 eV. This comparison shows that the OER preferably occurs in $MnO_2$ sample instead of $Mn_{1-x}Cr_xO_2$. Interestingly, the assembled Ru atoms on $MnO_2$ (middle panel) or $Mn_{1-x}Cr_xO_2$ (bottom panel) will cause a spin-dependent electronic arrangement, greatly optimizing the corresponding catalytic activity. For Ru-$MnO_2$ sample (middle panel), the rate-limiting intermediate *OOH remains unchanged, but the activation energy decreased from 1.19 eV (LS) to 0.67 eV (HS) with the flipping of a spin state electron. If Ru atoms are selectively assembled onto $Mn_{1-x}Cr_xO_2$ surface (bottom panel), the activation energy further decreased to 0.63 eV at HS, because microwave-mediated spin-dependent symmetry-breaking leads to a multilevel orbital hybridization and electron rearrangement facilitating the electronic "acceptance-donation" process. By the way, the possibility that the Mn sites around the Ru atoms act as adsorption-activating centers has been ruled out (Supplementary Figs. 60 and 61).

Spin-dependent orbital hybridization and charge transfer were compared from the charge density difference for Ru-$Mn_{1-x}Cr_xO_2$ with adsorbed *OOH species (Fig. 5d). The charge reconfiguration is mainly delocalized at the formed Ru−OOH bonds, especially for the HS state. The Ru site with HS configuration donates sufficient unpaired *d*-electrons to the formed Ru−OOH bonds, leading to an energetic bonding interaction from *d-p* orbital hybridization. Bader charge analysis also confirms that the Ru sites at HS lead to a charge transfer of 0.034 e, larger than the charge transfer of LS (0.022 e). To better understand this process, the crystal orbital Hamilton population (COHP) was compared (Fig. 5e). Unlike the HS configuration, an obvious antibonding interaction appears at the Fermi levels. This makes the LS configuration challenging to optimize the electron donation process, leading to a higher rate-limiting potential barrier. The differences in bonding interactions can also be quantitatively evaluated from the integrated area of COHP (ICOHP). The higher electron orbital overlap (lower ICOHP) at HS (−1.07 eV) than LS (−0.96 eV) indicates stronger Ru−OOH orbital interaction. Meanwhile, an easier charge transfer and orbital hybridization preferably choose the HS configuration. The experimental and theoretical analyses confirm that microwave-mediated symmetry-breaking-dependent orbital degeneracy and spin electronic rearrangement play a crucial role in enhancing the reaction kinetics and stability of acidic OER (Supplementary Fig. 62).

### PEM−WE device performance

Motivated by the superior acidic OER activity and stability of $Ru_{MW}$-$Mn_{1-x}Cr_xO_2$, we proceeded to assess its practical water-splitting potential. Herein, $Ru_{MW}$-$Mn_{1-x}Cr_xO_2$ was used as the anode catalyst for OER, commercial Pt/C as the cathode catalyst for HER, and a PEM to construct a PEM-WE electrolyzer (Fig. 6a and Supplementary Fig. 63). The membrane electrode assembly (MEA) was prepared using the catalyst-coated membrane (CCM) method (Supplementary Figs. 64 and 65). The SEM image and corresponding EDS mapping (Fig. 6b) clearly show the microstructure of MEA composed of Pt/C and $Ru_{MW}$-$Mn_{1-x}Cr_xO_2$ catalysts, tightly and uniformly distributed on both sides of PEM. The zero-gap electrode interface is beneficial for accelerating proton migration and charge transport between the anode and cathode. The steady-state current−voltage (I−V) polarization curves (without *iR* compensation) (Fig. 6c) clearly show that $Ru_{MW}$-$Mn_{1-x}Cr_xO_2$ had greater water electrolysis activity compared to the com-$RuO_2$ catalyst. At 80 °C, cell voltages of only 1.67 and 1.88 V were required to reach current densities of 0.5 and 1.0 A $cm^{-2}$, respectively, far superior to those achievable with com-$RuO_2$ (1.99 V@0.5 A $cm^{-2}$ and 2.49 V@1.0 A $cm^{-2}$). More importantly, the $Ru_{MW}$-$Mn_{1-x}Cr_xO_2$ cell can be operated stably at 0.2 and 1.0 A $cm^{-2}$ over 300 h (Fig. 6d), with a negligible degradation rate (~0.18 mV $h^{-1}$), substantially better than the com-$RuO_2$ electrolyzer (0.2 A $cm^{-2}$, <30 h). The $Ru_{MW}$-$Mn_{1-x}Cr_xO_2$ electrolyzer exhibits stronger stability at higher current densities compared to the other state-of-the-art electrocatalysts (Supplementary Table 8). In addition, there was no apparent change in the morphology and electronic structure of the catalysts on MEA after long-term operation in the PEM electrolyzer (Supplementary Figs. 66 and 67), further corroborating the notable durability of the $Ru_{MW}$-$Mn_{1-x}Cr_xO_2$ catalyst under industrially relevant harsh scenarios.

Subsequently, we compared the energy indicators of different electrolyzers to quantify their application value, as electricity costs account for 50–90% of the overall levelized cost of hydrogen production. As shown in Fig. 6e, the well-designed $Ru_{MW}$-$Mn_{1-x}Cr_xO_2$ cell exhibits substantial improvements in energy utilization, including power consumption per cubic meter of hydrogen yield (W) of 3.65 kW h $Nm^{-3}$, electricity-to-hydrogen energy conversion efficiency (ETH) of 88.7%, hydrogen production rate (*R*) of 3.64 $Nm^3$ $h^{-1}$ $m^{-2}$, and current density at 1.8 V (*j*) = 797 mA $cm^{-2}$. These values are notably superior compared to a typical com-$RuO_2$ electrolyzer, which has W of 4.35 kW h $Nm^{-3}$, ETH of 74.4%, *R* of 1.36 $Nm^3 h^{-1} m^{-2}$, and *j* of 298 mA $cm^{-2}$. More importantly, the cost per gallon of gasoline equivalent (GGE) for the $H_2$ produced using a $Ru_{MW}$-$Mn_{1-x}Cr_xO_2$ electrolyzer is only USD 0.87, far below the U.S. Department of Energy' s 2026 target of US$ 2.00[64]. Additionally, the scalability and cost of electrocatalysts are crucial for practical applications. The $Ru_{MW}$-$Mn_{1-x}Cr_xO_2$ catalyst can be synthesized on a gram scale using a custom microwave reactor (Supplementary Fig. 68), with a calculated cost of approximately USD 2001 per kg. This is only 4.9% of the cost of com-$RuO_2$ (approximately USD 40,383 per kg) and 0.47% of $IrO_2$ (approximately USD 428,000 per kg) (Supplementary Tables 9 and 10). Considering both cell performance and noble metal cost, the advantages of the microwave-mediated orderly Ru atomic assembly and spin renormalization are clear. Moreover, owing to its intrinsic fast proton transport, the PEM-WE has a much faster start-up and shut-down response than other electrolyzer types like alkaline water electrolyzers and anion exchange membrane electrolyzers. Consequently, our $Ru_{MW}$-$Mn_{1-x}Cr_xO_2$ cell performs well with variable energy sources such as wind, photovoltaic, and thermoelectric power in experiments (Supplementary Fig. 69). More crucially, utilizing these clean energy sources to drive the PEM-WE can further reduce carbon emissions, promoting a closed-loop carbon footprint and sustainable social development.

## Discussion

To summarize, we developed a microwave-mediated strategy that selectively assembles Ru patterns onto the $Mn_{1-x}Cr_xO_2$ surface. Microwave-modulated coherent energy superposition avoids random agglomerations in Ru atomic assembly while inducing localized spin domain renormalization, enhancing Ru sites' reactivity and preventing deleterious overoxidation in acidic OER. The obtained $Ru_{MW}$-$Mn_{1-x}Cr_xO_2$ catalyst possesses a high mass activity of 1014.5 A $g_{Ru}^{-1}$, which is about 33-fold higher than the $Ru_T$-$Mn_{1-x}Cr_xO_2$ processed through traditional heating. Moreover, $Ru_{MW}$-$Mn_{1-x}Cr_xO_2$

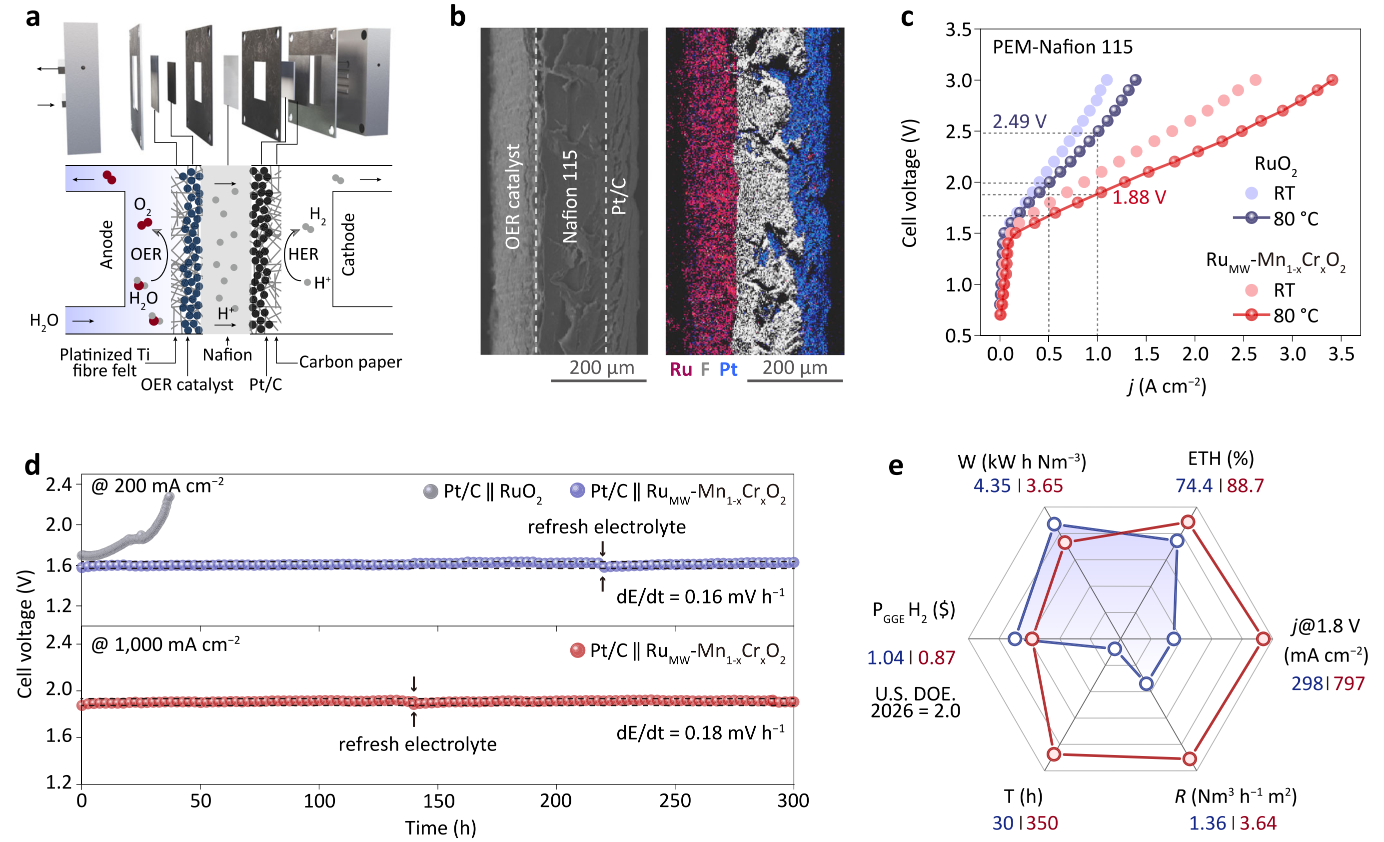

**Fig. 6 | PEM electrolyzer performance using $Ru_{MW}$-$Mn_{1-x}Cr_xO_2$ as anode electrocatalyst.** **a** Schematic of the stack structure and operation principle for the PEM electrolyzer. **b** The SEM image and corresponding elemental mapping of the MEA prepared by the CCM process. **c** Polarization curves of the PEM electrolyzer using $Ru_{MW}$-$Mn_{1-x}Cr_xO_2$ or com-$RuO_2$ as the anodic catalyst and commercial Pt/C as the cathodic catalyst, at room temperature (RT) and 80 °C. No cell voltages were *iR* compensated. **d** Top panel: Chronopotentiometry curves of the PEM electrolyzer using $Ru_{MW}$-$Mn_{1-x}Cr_xO_2$ or com-$RuO_2$ catalyst operated at 200 mA $cm^{-2}$. Bottom panel: Chronopotentiometry curve of the PEM electrolyzer using $Ru_{MW}$-$Mn_{1-x}Cr_xO_2$ catalyst operated at 1000 mA $cm^{-2}$. **e** Comprehensive comparison of the PEM electrolyzer using $Ru_{MW}$-$Mn_{1-x}Cr_xO_2$ (red line) and com-$RuO_2$ catalysts (blue line) in terms of the W, ETH (500 mA $cm^{-2}$), *j* (at 1.8 V), *R*, T, and per GGE $H_2$ price. W, power consumption per cubic meter of hydrogen yield; ETH, electricity-to-hydrogen energy conversion efficiency; *j*, current density; *R*, hydrogen production rate; GGE, gallon of gasoline equivalent.

demonstrates an industrial current density of 1.0 A $cm^{-2}$ at 1.88 V cell voltage and operates stably over 300 h in a PEM electrolyzer. The higher electrolysis efficiency and lower comprehensive cost further demonstrate that the PEM system using the $Ru_{MW}$-$Mn_{1-x}Cr_xO_2$ catalyst has great future potential in practical water splitting to produce green hydrogen. From both theoretical research and practical application perspectives, this work suggests an intriguing nanotechnology to realize the orderly assembly and spin configuration optimization of Ru atomic patterns, thereby boosting the acidic water oxidation performance.

# Methods

### Synthesis of α-$MnO_2$ and Cr-doped $MnO_2$

To synthesize α-$MnO_2$ nanofibers, 0.02 mol of $MnSO_4{\cdot}H_2O$, 0.02 mol of $(NH_4)_2S_2O_8$, and 0.06 mol of $K_2SO_4$ were dissolved in 70 mL of $H_2O$. The mixture was stirred vigorously for 1 h, transferred to an autoclave, and heated at 140 °C for 12 h. After cooling to room temperature, the resulting dark brown powders were washed alternately five times with deionized water and ethanol, separated via vacuum filtration, and dried overnight in an oven at 60 °C. To generate Cr-doped $MnO_2$, varying amounts of $CrCl_3$ (0.5%, 1%, 3%, and 5% of Mn's molar mass) were added to the solution. These were designated as $Mn_{1-x}Cr_xO_2$ (x represents 0.005, 0.01, 0.03, and 0.05, respectively). Unless otherwise stated, 1% Cr-doped $MnO_2$ was referred to as $Mn_{1-x}Cr_xO_2$ in this work. The precise Cr content in bulk $MnO_2$ was determined using ICP-OES.

### Microwave-mediated Ru atomic pattern assembly

For the assembly of Ru atomic patterns, 50 mg of as-prepared $Mn_{1-x}Cr_xO_2$ nanofibers and 40 mg of $RuCl_3{\cdot}xH_2O$ were each dispersed in 10 mL of $H_2O$ and sonicated for 30 min. The two solutions were then thoroughly mixed and injected into a polytetrafluoroethylene microwave reactor. The mixture was heated in a microwave oven (2.45 GHz, 900 W) for 0.5 h. The microwave time and microwave power were optimized in Supplementary Fig. 13. After naturally cooling to room temperature, the product was separated by vacuum filtration, washed alternately with ethanol and deionized water, and dried overnight in a vacuum oven at 80 °C to obtain microwave-assisted Ru-assembled $Mn_{1-x}Cr_xO_2$ ($Ru_{MW}$-$Mn_{1-x}Cr_xO_2$). Microwave-assisted Ru assembly on $MnO_2$ substrates ($Ru_{MW}$-$MnO_2$) followed a similar process. To differentiate the effects of microwave-mediated coherent energy superposition from traditional heating on Ru pattern assembly, thermal-assisted Ru assembly samples ($Ru_T$-$MnO_2$ and $Ru_T$-$Mn_{1-x}Cr_xO_2$) were prepared using an oil bath device at 100 °C, matching the theoretical temperature of microwave heating.

### Electrochemical measurements

The OER tests were conducted through a standard three-electrode system on an electrochemical workstation (Autolab PGSTAT302N, Metrohm). The $O_2$-saturated $HClO_4$ electrolyte of 0.1 M was freshly prepared before each test and stored at room temperature. All glassware was sonicated in ultrapure water before electrochemical treatment. Ag/AgCl (saturated KCl) served as the reference electrode, and a graphite rod (99.99%, Ledonlab) as the counter electrode. The reference electrode was calibrated in hydrogen-saturated 0.01 M $HClO_4$. The calibrated value for Ag/AgCl in 3.5 M AgCl−KCl was equal to 0.211 (close to the theoretical value of 0.205). The catalyst ink was prepared by dispersing the as-prepared catalyst (5 mg) with Vulcan XC-72 (2.5 mg) into 1 mL of mixed solution (5% Nafion® solution/deionized water/ethanol = 2:73:25 by volume). The effect of adding carbon black was discussed in detail in Supplementary Fig. 70. After 1 h of sonication, 50 µL of homogeneous ink was dropped onto a carbon paper electrode (geometric area: 0.5 $cm^2$), resulting in a catalyst loading of 0.5 mg $cm^{-2}$, and dried fully in air at room temperature to serve as the working electrode. LSV with a scanning rate of 5 mV $s^{-1}$ was conducted in the potential range of 1.15–1.75 V versus RHE. Measurements were repeated at least three times using freshly deposited catalysts to assess reproducibility. All potentials measured against Ag/AgCl were converted to the RHE scale using: $E$ (potential, versus RHE) = $E$ (versus Ag/AgCl) + $E^o$ (versus Ag/AgCl) + 0.059 × pH. In 0.1 M $HClO_4$ electrolyte, pH values are ~0.9 ± 0.04. $E$-$iR$ represents 95% $iR$-corrected, where $i$ is the measured current and $R$ is the uncompensated solution resistance (~10 ± 0.8 Ω) as obtained from EIS. EIS measurements were carried out in the frequency range of 100 kHz to 0.1 Hz, applying different overpotentials. Stability tests were performed using chronopotentiometry (CP) measurements at 10 mA $cm^{-2}$ for 200 h. During LSV and CP tests, the electrolyte was stirred magnetically at 900 rpm to accelerate the detachment of oxygen bubbles on the working electrode surface. The Tafel plot was obtained by converting the J-V curves to potential (V versus RHE) versus the logarithm of current density (log |J|). Pulse voltammetry was performed to monitor the current over time. The potential was maintained at a low potential ($E_{low}$ = 1.15 V versus RHE) for 5 s, then switched to a higher potential ($E_{high}$) for 5 s, before returning to $E_{low}$ for 5 s. This cycle was repeated, increasing $E_{high}$ from 1.27 V to 1.59 V in 20 mV increments. The charge related to the potential step was calculated by integrating the current pulse over time after subtracting the background current signal (OER current). The OER current was recorded at the end of the 5 s anodic potential segment.

### PEM water electrolyzer tests

The MEA was prepared using the classical CCM method. $Ru_{MW}$-$Mn_{1-x}Cr_xO_2$ or commercial $RuO_2$ (a typical OER catalyst) was used as the OER anode catalyst, and commercial Pt/C (40 wt%) was used as the HER cathode catalyst. Catalysts were dispersed in a mixture of isopropanol and distilled water (7:1) with 20 wt.% Nafion 117 ionomer for the cathode and 30 wt.% for the anode. The mixture was sonicated in a low-temperature water bath for at least 1 h and filtered through a 500-mesh filter to obtain a homogeneous catalyst ink. Then, around 1 mg $cm^{-2}$ of commercial Pt/C and 2.5 mg $cm^{-2}$ of $Ru_{MW}$-$Mn_{1-x}Cr_xO_2$ with carbon black catalysts (3:1) were uniformly air-sprayed onto both sides of the Nafion 115 membrane (thickness: ~130 µm) under heating conditions. Finally, platinized titanium fiber felt (0.4 mm) and carbon paper were used as the porous transport layers in the anode and cathode, which were hot-pressed together with MEA (135 °C, 30 MPa) for 8 min. Deionized water was circulated in the anode using a peristaltic pump at 10 rpm. The electrolyzer's operating temperature is regulated by the thermostat water bath and resistance heating element. Steady-state polarization curves and chronopotentiometric curves were obtained using a programmable direct-current power supply (DAHUA, DH1790-1).

### Computational details

All DFT calculations were performed by the Vienna Ab initio Simulation Package[65]. The electronic structures of materials were described by the generalized gradient approximation exchange-correlation function with Perdew–Burke–Ernzerhof (PBE)[66]. Monkhorst–Pack k-points grid of 9 × 9 × 1 was applied to expand the Kohn–Sham wave functions. The plane wave basis set had a cutoff energy of 500 eV. A vacuum space of 20 Å was used for all the slab models (Supplementary Data 1) to ensure the periodic images were well separated. The bottom two layers of atoms in the slabs were fixed to mimic bulk, and then the surface relaxations were performed. The geometry relaxation and energy convergence tolerance for the electronic structure were 0.01 eV $Å^{-1}$ and $10^{-5}$ eV per atom, respectively. Spin polarization was applied to all structures. More computational details about formation energy and solvation effects were provided in the Supplementary Methods.

## Data availability

Source data are available via Figshare (https://doi.org/10.6084/m9.figshare.27645825)[67].

## References

1. Wolfram, P. et al. The hydrogen economy can reduce costs of climate change mitigation by up to 22. *One Earth* **7**, 885–895 (2024).
2. Chong, L. et al. La- and Mn-doped cobalt spinel oxygen evolution catalyst for proton exchange membrane electrolysis. *Science* **380**, 609–616 (2023).
3. Henkensmeier, D. et al. Separators and membranes for advanced alkaline water electrolysis. *Chem. Rev.* **124**, 6393–6443 (2024).
4. Liu, R.-T. et al. Recent advances in proton exchange membrane water electrolysis. *Chem. Soc. Rev.* **52**, 5652–5683 (2023).
5. Chatenet, M. et al. Water electrolysis: from textbook knowledge to the latest scientific strategies and industrial developments. *Chem. Soc. Rev.* **51**, 4583–4762 (2022).
6. Johnson Matthey Price Charts (Johnson Matthey); www.platinum.matthey.com/prices/pricecharts#.
7. Hao, S. et al. Torsion strained iridium oxide for efficient acidic water oxidation in proton exchange membrane electrolyzers. *Nat. Nanotechnol.* **16**, 1371–1377 (2021).
8. Su, H. et al. Tensile straining of iridium sites in manganese oxides for proton-exchange membrane water electrolysers. *Nat. Commun.* **15**, 95 (2024).
9. Chen, D. et al. Bicontinuous $RuO_2$ nanoreactors for acidic water oxidation. *Nat. Commun.* **15**, 3928 (2024).
10. Shi, Z. et al. Customized reaction route for ruthenium oxide towards stabilized water oxidation in high-performance PEM electrolyzers. *Nat. Commun.* **14**, 843 (2023).
11. Wang, J. et al. Exceptionally active and stable $RuO_2$ with interstitial carbon for water oxidation in acid. *Chem* **8**, 1673–1687 (2022).
12. Zhao, G. et al. Metallic Ru-Ru interaction in ruthenium oxide enabling durable proton exchange membrane water electrolysis. *Adv. Mater.* **36**, 2404213 (2024).
13. Gunasooriya, G. T. K. K. et al. Analysis of acid-stable and active oxides for the oxygen evolution reaction. *ACS Energy Lett.* **5**, 3778–3787 (2020).
14. Cui, X. et al. Robust interface Ru centers for high-performance acidic oxygen evolution. *Adv. Mater.* **32**, 1908126 (2020).
15. Qin, Y. et al. $RuO_2$ electronic structure and lattice strain dual engineering for enhanced acidic oxygen evolution reaction performance. *Nat. Commun.* **13**, 3784 (2022).
16. Ping, Y. et al. The reaction mechanism with free energy barriers at constant potentials for the oxygen evolution reaction at the $IrO_2$ (110) surface. *J. Am. Chem. Soc.* **139**, 149–155 (2017).
17. Zhang, Y. et al. Rational design of cost-effective metal-doped $ZrO_2$ for oxygen evolution reaction. *Nano-Micro Lett.* **16**, 180 (2024).
18. Li, G. et al. Dual hydrogen production from electrocatalytic water reduction coupled with formaldehyde oxidation via a copper-silver electrocatalyst. *Nat. Commun.* **14**, 525 (2023).
19. Sun, Y. et al. Spin-related electron transfer and orbital interactions in oxygen electrocatalysis. *Adv. Mater.* **32**, 2003297 (2020).

20. Ren, X. et al. Spin-polarized oxygen evolution reaction under magnetic field. *Nat. Commun.* **12**, 2608 (2021).
21. Sun, Z. et al. Regulating the spin state of $Fe^{III}$ enhances the magnetic effect of the molecular catalysis mechanism. *J. Am. Chem. Soc.* **144**, 8204–8213 (2022).
22. Huang, J. et al. Surface oxidation/spin state determines oxygen evolution reaction activity of cobalt-based catalysts in acidic environment. *Nat. Commun.* **15**, 3067 (2024).
23. Zhang, Z. et al. Distance effect of single atoms on stability of cobalt oxide catalysts for acidic oxygen evolution. *Nat. Commun.* **15**, 1767 (2024).
24. Magnier, L. et al. Fe-Ni-based alloys as highly active and low-cost oxygen evolution reaction catalyst in alkaline media. *Nat. Mater.* **23**, 252–261 (2024).
25. Liu, S. et al. A top-down strategy for amorphization of hydroxyl compounds for electrocatalytic oxygen evolution. *Nat. Commun.* **13**, 1187 (2022).
26. Florek, W. et al. Universal lowest energy configurations in a classical Heisenberg model describing frustrated systems with wheel geometry. *Phys. Rev. B* **100**, 054434 (2019).
27. Gusev, V. V. et al. Optimality guarantees for crystal structure prediction. *Nature* **619**, 68–72 (2023).
28. Meng, Y.-S. et al. Manipulating spin transition to achieve switchable multifunctions. *Acc. Chem. Res.* **52**, 1369–1379 (2019).
29. Su, S.-Q. et al. Photoinduced persistent polarization change in a spin transition crystal. *Angew. Chem. Int. Ed.* **61**, e202208771 (2022).
30. Liu, L. et al. Metal catalysts for heterogeneous catalysis: from single atoms to nanoclusters and nanoparticles. *Chem. Rev.* **118**, 4981–5079 (2018).
31. Dong, C. et al. Engineering *d-p* orbital hybridization with P, S Co-coordination asymmetric configuration of single atoms toward high-rate and long-cycling lithium–sulfur battery. *Adv. Mater.* **36**, 2407070 (2024).
32. Sohail, M. et al. Recent progress in ruthenium-based electrocatalysts for water oxidation under acidic condition. *ACS Sustain. Chem. Eng.* **11**, 17564–17594 (2023).
33. Liu, M. et al. In situ modulating coordination fields of single-atom cobalt catalyst for enhanced oxygen reduction reaction. *Nat. Commun.* **15**, 1675 (2024).
34. Liu, M. et al. Tracking the role of compressive strain in bowl-Like Co-MOFs structural evolution in water oxidation reaction. *Appl. Catal. B Environ.* **354**, 124114 (2024).
35. Zhang, X. et al. High-spin $Co^{3+}$ in cobalt oxyhydroxide for efficient water oxidation. *Nat. Commun.* **15**, 1383 (2024).
36. Shimoyama, Y. et al. Oxygen evolution reaction driven by charge transfer from a Cr complex to Co-containing polyoxometalate in a porous ionic crystal. *J. Am. Chem. Soc.* **144**, 2980–2986 (2022).
37. Huang, P. et al. Dynamic orbital hybridization triggered spin-disorder renormalization via super-exchange interaction for oxygen evolution reaction. *Proc. Natl Acad. Sci. USA* **120**, e2219661120 (2023).
38. Khan, M. M. T. et al. Ruthenium(III) chloride in aqueous solution: kinetics of the aquation and anation reactions of the chloro complexes. *Inorg. Chem.* **27**, 3274–3278 (1988).
39. Guggemos, N. et al. Electric dipole moments of nanosolvated acid molecules in water clusters. *Phys. Rev. Lett.* **114**, 043401 (2015).
40. Li, H. et al. Fundamentals and applications of microwave heating to chemicals separation processes. *Renew. Sust. Energy Rev.* **114**, 109316 (2019).
41. Głowniak, S. et al. Advances in microwave synthesis of nanoporous materials. *Adv. Mater.* **33**, 2103477 (2021).
42. Ravets, S. et al. Coherent dipole–dipole coupling between two single Rydberg atoms at an electrically-tuned Förster resonance. *Nat. Phys.* **10**, 914–917 (2014).
43. Xiao, S. et al. Microwave-positioning assembly: structure and surface optimizations for catalysts. *Small Struct.* **3**, 2100169 (2022).
44. Zhang, M.-J. et al. Ultrafast solid-liquid intercalation enabled by targeted microwave energy delivery. *Sci. Adv.* **6**, eabd9472 (2020).
45. Zoppellaro, G. et al. Microwave energy drives “on-off-on” spin-switch behavior in nitrogen-doped graphene. *Adv. Mater.* **31**, 1902587 (2019).
46. Taqui Khan, M. M. et al. Ruthenium(III) chloride in aqueous solution: electrochemical and spectral studies. *Inorg. Chem.* **25**, 665–670 (1986).
47. Li, R. et al. Effects of metal ion on the water structure studied by the Raman O–H stretching spectrum. *J. Raman Spectrosc.* **40**, 1200–1204 (2009).
48. Zhang, H. et al. Promoting Cu-catalysed $CO_2$ electroreduction to multicarbon products by tuning the activity of $H_2O$. *Nat. Catal.* **6**, 807–817 (2023).
49. Yao, Y. et al. Engineering the electronic structure of single atom Ru sites via compressive strain boosts acidic water oxidation electrocatalysis. *Nat. Catal.* **2**, 304–313 (2019).
50. Wu, Y. et al. Lattice strain advances thermoelectrics. *Joule* **3**, 1276–1288 (2019).
51. Lin, Y. et al. Chromium-ruthenium oxide solid solution electrocatalyst for highly efficient oxygen evolution reaction in acidic media. *Nat. Commun.* **10**, 162 (2019).
52. Zhang, B. et al. A strongly coupled Ru-$CrO_x$ cluster–cluster heterostructure for efficient alkaline hydrogen electrocatalysis. *Nat. Catal.* **7**, 441–451 (2024).
53. Li, S. et al. Highly efficient anion exchange membrane water electrolyzers via chromium-doped amorphous electrocatalysts. *Nat. Commun.* **15**, 3416 (2024).
54. Rückriegel, A. et al. Phase diagram of the $J_1$-$J_2$ quantum Heisenberg model for arbitrary spin. *Phys. Rev. B* **109**, 184410 (2024).
55. Mu, C. et al. Rational design of spinel cobalt vanadate oxide $Co_2VO_4$ for superior electrocatalysis. *Adv. Mater.* **32**, 1907168 (2020).
56. Li, L. et al. Spin-polarization strategy for enhanced acidic oxygen evolution activity. *Adv. Mater.* **35**, 2302966 (2023).
57. Li, C. et al. Giant Zeeman splitting for monolayer nanosheets at room temperature. *J. Am. Chem. Soc.* **142**, 20616–20623 (2020).
58. Zhao, S. et al. Constructing regulable supports via non-stoichiometric engineering to stabilize ruthenium nanoparticles for enhanced pH-universal water splitting. *Nat. Commun.* **15**, 2728 (2024).
59. Zhu, W. et al. Stable and oxidative charged Ru enhance the acidic oxygen evolution reaction activity in two-dimensional ruthenium-iridium oxide. *Nat. Commun.* **14**, 5365 (2023).
60. Nong, H. N. et al. Key role of chemistry versus bias in electrocatalytic oxygen evolution. *Nature* **587**, 408–413 (2020).
61. Lin, C. et al. In-situ reconstructed Ru atom array on α-$MnO_2$ with enhanced performance for acidic water oxidation. *Nat. Catal.* **4**, 1012–1023 (2021).
62. Wu, Z.-Y. et al. Non-iridium-based electrocatalyst for durable acidic oxygen evolution reaction in proton exchange membrane water electrolysis. *Nat. Mater.* **22**, 100–108 (2023).
63. Chang, J. et al. Oxygen radical coupling on short-range ordered Ru atom arrays enables exceptional activity and stability for acidic water oxidation. *J. Am. Chem. Soc.* **146**, 12958–12968 (2024).
64. U.S. Department of Energy. DOE national clean hydrogen strategy and roadmap. https://www.hydrogen.energy.gov/pdfs/clean-hydrogen-strategy-roadmp.pdf (2022).
65. Kresse, G. et al. Efficient iterative schemes for ab initio total-energy calculations using a plane-wave basis set. *Phys. Rev. B* **54**, 11169 (1996).
66. Perdew, J. P. et al. Generalized gradient approximation made simple. *Phys. Rev. Lett.* **77**, 3865–3868 (1996).

67. Shi, Y. et al. Source data for 'Electron–phonon coupling and coherent energy superposition induce spin-sensitive orbital degeneracy for enhanced acidic water oxidation'. figshare https://doi.org/10.6084/m9.figshare.27645825 (2025).

## Acknowledgements

This work was supported by National Natural Science Foundation of China (22274084, Y.H.X.; 12174183, L.Z.L.), Natural Science Foundation for Distinguished Young Scholars of Shandong Province (ZR2021JQ04, Y.H.X.), Taishan Scholars Program of Shandong Province (No. tsqn 201909088, Y.H.X.), Natural Science Foundation of Hebei Province (B2024205035, L.Z.L.) and a grant (BCIC-23-K4, L.Z.L.) from Guangxi Key Laboratory of Brain-inspired Computing and Intelligent Chips. This work was supported by High Performance Computing Centers of Shenzhen.

## Author contributions

Y.F.S., L.Z.L., and Y.H.X. conceived the idea. Y.F.S., L.P.W., M.L. performed the experiments and collected the data. Y.F.S., Z.Z.X., and P.L.H. analyzed the data. Y.F.S. plotted the figures. L.Z.L. carried out DFT simulations. Y.F.S., L.Z.L., and Y.H.X. completed the original draft writing. Y.F.S., L.Z.L., and Y.H.X. contributed to the writing-review and editing.

## Competing interests

The authors declare no competing interests.

## Additional information

**Supplementary information** The online version contains supplementary material available at https://doi.org/10.1038/s41467-025-56315-w.

**Correspondence** and requests for materials should be addressed to Lizhe Liu or Yuanhong Xu.

**Peer review information** *Nature Communications* thanks Zheng-Long Xu and the other anonymous reviewer(s) for their contribution to the peer review of this work. A peer review file is available.